Choosing Poses For Force and Stiffness Control

Arash Ajoudani, Nikos G. Tsagarakis, and Antonio Bicchi

***Abstract*— In humanoids and other redundant robots interacting with the environment, one often can choose between different configurations and control parameters to achieve a given task. A classical tool to describe specifications of the desired force/displacement behavior in such problems is the stiffness ellipsoid, whose geometry is affected by the choice of parameters in both joint control and redundancy resolution - namely, gains and angles. As is well known, impedance control techniques can regulate gains to realize any desired shape of the Cartesian stiffness ellipsoid at the end-effector, so that robot geometry selection could appear secondary. However, humans do not use this possibility: to control the stiffness of our arms, we predominantly use arm configurations. Why is that, and does it make sense to do the same in robots?**

To understand this discrepancy, we provide a more complete analysis of the task-space force/deformation behavior of compliant redundant arms to illustrate why the arm geometry plays a dominant role in interaction capabilities of robots. We introduce the notion of allowable Cartesian force/displacement ("stiffness feasibility") regions (SFR) for compliant robots with given torque boundaries. We show that different robot configurations modify such regions and explore the role of robot geometry in achieving an appropriate SFR for the task at hand. The novel concepts and definitions are first illustrated in simulations. Experimental results are then provided to verify the effectiveness of the proposed Cartesian force and stiffness control.

I. Introduction

Impedance control is a well-known technique to guarantee contact stability in robots by generating task-adapted restoring forces in response to the environmental displacements. In a quasi-static setting, the desired response in different directions, often represented by the stiffness ellipsoid [1], can be achieved by varying the joint control parameters and the geometry of the robot. Due to this geometric dependence, endpoint stiffness is subject to variations depending on the position of the endpoint in task space, or even on the robot configuration for the same end-effector (e-e) position, when the robot is redundant.

It is known that in principle, any arbitrary endpoint stiffness matrix can be realized in any arbitrary robot configuration [2]. With that being said, the control of robot configuration might appear unnecessary at first. However, to achieve an arbitrary stiffness matrix, the desired endpoint force/displacement relationship must be mathematically mapped to the joint–space which requires in general that the torque commanded at any joint depends on the robot geometry and the displacement of all joints in a tightly coupled way [3], [4]. On the other hand, a dense body of literature reports on the tendency of humans to explore the major role of configuration to achieve a certain physical interaction behavior [5]–[7]. A simple example in which a particular arm configuration (right posture) is intuitively chosen by humans over the other possible solutions (e.g. left posture) to oppose to the deformations with high restoring forces in a certain direction is demonstrated in Fig. 1 top two plots.

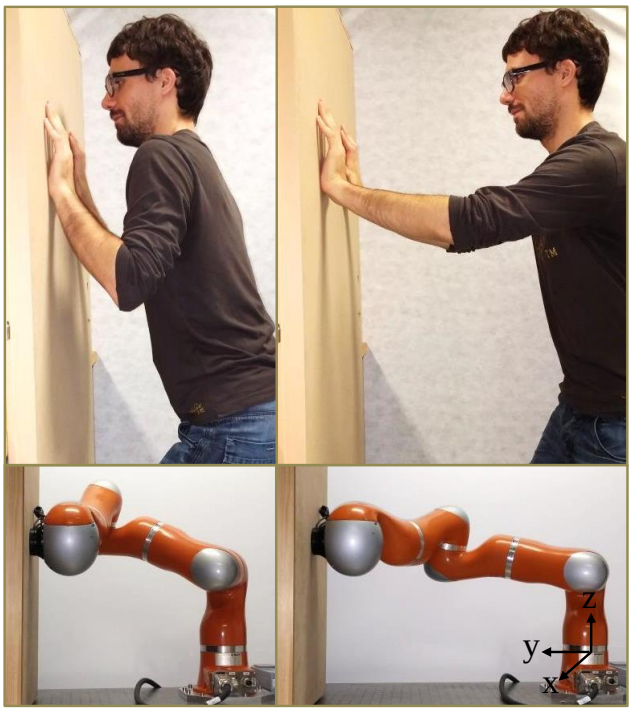

Fig. 1: Humans intuitively choose the configuration of their arms to obtain a desired impedance: e.g. to oppose more rigidly to an object motion, the configuration on the right is preferred to the one on the left. The second row shows a robot arm in roughly similar poses. Although, in principle, the robot's stiffness ellipsoid can be the same for both poses [2], there are reasons why the configuration on the right is better also for robots. This paper discusses why.

To investigate the effect of robot configuration on task-force capabilities, force ellipsoid was initially introduced in [8] as the preimage of the unit sphere in the joint torque space under a mapping which is defined by the robot geometry. The effect of robot mass and payload which contribute to a pure translation of the force ellipsoid in the task space has also been addressed [9]. Notwithstanding the widespread use of force ellipsoids, they can be imprecise due to the

Arash Ajoudani, Nikos G. Tsagarakis and Antonio Bicchi are with the Dept. of Advanced Robotics, Istituto Italiano di Tecnologia, Via Morego 30, 16163, Genova, Italy. e-mails: arash.ajoudani@iit.it, nikos.tsagarakis@iit.it and bicchi@centropiaggio.unipi.it.

This work is supported in part by the European Research Council under the Advanced Grant SoftHands "A Theory of Soft Synergies for a New Generation of Artificial Hands" no. ERC-291166, and EU FP7-ICT project, WALKMAN, "Whole-body Adaptive Locomotion and Manipulation", no. 611832.

fact that in such a representation the dynamic boundaries, e.g. the actuators' torque limits, are not taken into account. As an alternative solution, the use of force polytopes was recommended that account for exact maximum achievable task space force, subject to the imposed constraints in the space of joint torques [10].

It is important to note here that both the above representations only convey a local picture of the robot's capabilities. In a compliant robot, where the aim is to achieve a desired displacement-force relationship, applied external disturbance will modify the robot configuration, and the corresponding force polytope as a consequence. This implies that linear bounds on joint torques will not be translated into linear bounds on Cartesian forces: one of the objectives of this paper is to address this problem and demonstrate that the Cartesian force boundary of a compliant robot in an arbitrary configuration has a nonpolytopic shape in general.

Now assume that a Cartesian stiffness controller in a torque controlled robot under gravity is implemented to achieve a desired stiffness matrix, in a particular configuration. This is associated with a maximum allowable displacement region, after reaching which, some actuators will hit the boundaries in the space of joint torques and the equilibrium assumption will no longer be valid. Noteworthy, the actuators' torque saturation under the Cartesian stiffness control will occur later for some configurations than for others[1]: this is the next topic we would like to investigate and capture with our measure. We demonstrate that even though a torque controlled robot in an arbitrary configuration is capable of realizing any shape of the stiffness ellipsoid at the e-e, a particular joint geometry renders the most effective interaction performance compared to the others. Here, the desired interaction performance is defined by the robot capability to confront large disturbance force/displacement profiles prior to the occurrence of torque saturation. This is achieved by realizing a displacement boundary region in Cartesian coordinates which is maximally aligned with the direction of the external disturbance and minimally translated due to the effect of gravity.

It is important to note here that a preliminary version of this work has been presented in [11]. The current study introduces significant improvements to the previous results by i- reformulation of the manipulator dynamics in the presence of external load and gravity, ii- providing deeper discussions on the proposed concepts and techniques, and iii- presenting new experimental results in a realistic task.

The rest of the paper is structured as follows: performance limits of the Cartesian stiffness control for nonredundant and redundant manipulators are described in Sections II and III, respectively. The use of robot redundancy to achieve a task-appropriate interaction performance is discussed in section IV and experimentally validated in section V. Finally, section VI presents the conclusions.

[1]For instance, for a similar Cartesian stiffness matrix, the robot configuration on the right in Fig. 1 can generate higher restoring forces in response to the environmental displacement in y direction, compared to the one on the left.

II. Interaction Boundaries of the Cartesian Force and Stiffness Control – Nonredundant Case

Consider the robot with forward kinematic map $x=\Lambda(q)$ initially at equilibrium $E(q_0,\tau_0,f_0)$ with $x_0=\Lambda(q_0)$ and $\tau_0=J^T(q_0)f_0+\tau_g(q_0)$, and a nearby equilibrium $E(q_0+\delta q,\tau_0+\delta\tau,f_0+\delta f)$, with $x_0+\delta x=\Lambda(q_0+\delta q)$ and $\tau_0+\delta\tau=J^T(q_0+\delta q)(f_0+\delta f)+\tau_g(q_0+\delta q)$. Here, x, f, q, τ, and τ_g denote the Cartesian position/orientation, Cartesian force, joint angle, joint torque and gravity vectors, respectively. The infinitesimal increment of these variables are expressed by δ. The manipulator Jacobian is represented by $J\in\mathbb{R}^{m\times n}$, with n being the number of joints and m corresponding to the task space dimension (where for nonredundant case $m=n$).

Assume that the aim is to achieve a desired restoring force profile, $\delta f(x,x_0)$, in the task space. By taking a first order Taylor expansion, we can write

$$\begin{aligned}\tau_0+\delta\tau &= J^T(q_0+\delta q)\,(f_0+\delta f)+\tau_g(q_0+\delta q)\\ &\approx J^T(q_0)f_0+\left.\tfrac{\partial J(q)^T f_0}{\partial q}\right|_{q_0,f_0}\delta q+J^T(q_0)\delta f\\ &+ \left.\tfrac{\partial J(q)^T\delta f}{\partial q}\right|_{q_0,f_0}\delta q+\tau_g(q_0)+\left.\tfrac{\partial \tau_g(q)}{\partial q}\right|_{q_0,f_0}\delta q,\end{aligned} \tag{1}$$

with the fourth term in the above equation being negligible, hence

$$\delta\tau=J^T(q_0)\delta f+\left.\frac{\partial J^T f_0}{\partial q}\right|_{q_0}\delta q+\left.\frac{\partial \tau_g(q)}{\partial q}\right|_{q_0}\delta q.$$

In addition, as regards the gravitational term, we can write

$$\tau_g(q)=\sum_{i=1}^{n}J_{com_i}^T f_{g_i}, \tag{2}$$

with $f_{g_i}=gm_i$, where J_{com_i}, m_i and g are the centre of mass Jacobian, the mass of the ith link, and vector of gravitational accelerations, respectively. Therefore

$$\delta\tau=J^T(q_0)\delta f+\left.\frac{\partial J^T f_0}{\partial q}\right|_{q_0}\delta q+\sum_{i=1}^{n}\left.\frac{\partial J_{com_i}^T(q)gm_i}{\partial q}\right|_{q_0}\delta q.$$

The basic idea of the impedance control is to find a control law ($\delta\tau$) such that the desired force profile (δf) is realized. Even though it is difficult to determine such a generally nonlinear update law, it can be done using 1st-order approximations, i.e. $\delta f=K_c\delta x$, with K_c denoting the stiffness matrix. Thus, the corresponding torque to be commanded at the joints can be computed by

$$\begin{aligned}\delta\tau &= [J^T(q_0)K_c+\left.\tfrac{\partial J(q)^T f_0}{\partial q}\right|_{q_0}J^{-1}(q_0)\\ &+ \sum_{i=1}^{n}\left.\tfrac{\partial J_{com_i}^T(q)gm_i}{\partial q}\right|_{q_0}J^{-1}(q_0)]\delta x.\end{aligned} \tag{3}$$

Note that the above equation is only valid for small displacements around the initial equilibrium point. For a relatively large deformation of the manipulator's e-e, the generally nonlinear association between the manipulator's joint torque and Cartesian force vector can be represented by series of re-linearized quasi-static equations for each

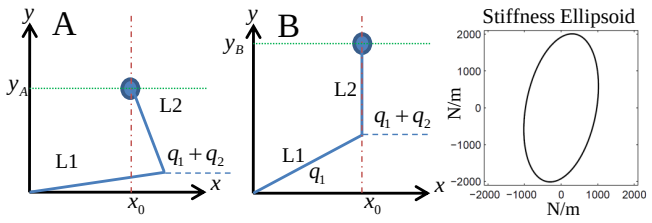

Fig. 2: Two-link manipulator in configuration A (left) and B (middle). Even if both configurations realize a similar desired Cartesian stiffness profile (most right plot), interaction Boundaries of the Cartesian force/stiffness control in the presence of external disturbance are different.

nearby equilibrium pair within the continuous closed interval[2] $[x_0\ x_1\ \cdots\ x_k\ \cdots\ x_{n_{eq}}]$, with $\tau_i = J^T(q_i)f_i + \tau_g(q_i)$, and $i = 1,2,...,n_{eq}$. Using a similar technique as in (1) and (3), at each step, the additional joint torque can be calculated using the current measurements as follows

$$\begin{aligned}\delta\tau_k &= [J^T(q_{k-1})K_c + \frac{\partial J(q)^T f_{k-1}}{\partial q}\Big|_{q_{k-1}} J^{-1}(q_{k-1}) \\ &+ \sum_{i=1}^{n} \frac{\partial J^T_{com_i}(q) g m_i}{\partial q}\Big|_{q_{k-1}} J^{-1}(q_{k-1})]\delta x_k,\end{aligned} \tag{4}$$

with $k-1$ and k denoting the index numbers which correspond to the two nearby equilibriums $E(q_{k-1},\tau_{k-1},f_{k-1})$ and $E(q_k,\tau_k,f_k)$. Equation (4) at each point must comply with the maximum achievable task space forces and velocities for given limits in the joint space[3] [8], [10]. Otherwise, certain values of external force/displacement will cause torque saturation and as a consequence, the equilibrium condition assumption will no longer be valid and the realized stiffness behavior will not be as desired.

To illustrate the underlying concept, let's consider a two-link manipulator in configuration A as depicted in Fig. 2, left plot. Assume that the aim is to realize a desired stiffness matrix $K_{c_d} = \begin{bmatrix}1 & 0.2\\ 0.2 & 2\end{bmatrix}\frac{kN}{m}$, at the e-e of the robot. Here, $q_A = [10^o, 110^o]$, $L_1 = 0.14$m, $L_2 = 0.12$m, $|\tau_1| \leq 3$Nm, and $|\tau_2| \leq 2$Nm. The mass (m) of each link is assumed to be a point mass and located at the centre of mass of each link with $m_1 = 4$ and $m_2 = 2$ Kg. For small values of displacement profile along $-y$, restoring forces will demonstrate a linear trend. However, at a certain point (y = y_A, see Fig. 3), the actuator torque will saturate and from this point on, the force-displacement relation will not satisfy the equilibrium condition and the realized task stiffness will not be as desired. The computation of the Cartesian forces is achieved through the inverse of the Jacobian matrix ($J \in \mathbb{R}^{2\times 2}$, when invertible), in $F = J^{-1}(\tau - \tau_g)$. When the computed torque of an actuator (using (4)) is saturated, its closest value (maximum or minimum torque) is used for that component in the τ vector.

Now, consider the same manipulator in another configuration (B, $q_B = [31^o, 59^o]$, Fig. 2, middle plot), exposed to a similar external displacement profile. In this configuration, joint torques will exceed the limits at y = $y_B > y_A$, highlighting the fact that the actuation torque saturation while realizing a desired compliant profile will happen later for some configurations than for others. This simple example demonstrates why the choice of arm geometry can play an important role in interaction boundaries of the task force or stiffness control.

[2]Assuming that no singularity occurs in this boundary and the final point $x_{n_{eq}}$ is reachable.

[3]In this paper we only consider the dynamic boundaries of the robot. A detailed discussion on the mobility and manipulability of the robots regarding kinematic constraints can be found in [12].

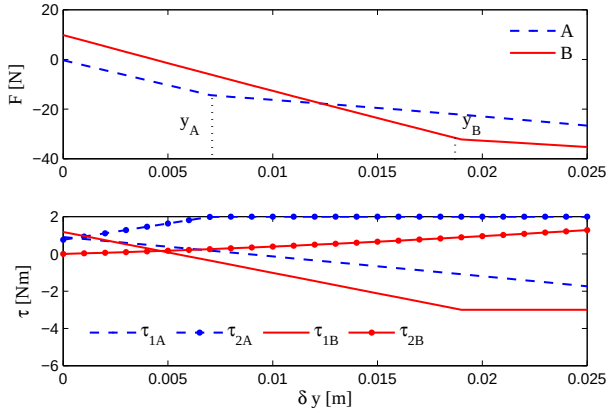

Fig. 3: Endpoint forces vs. displacements along $-y$ direction in manipulators A and B (upper plot), and the corresponding joint torques (lower plot). Initial force offsets refer to the effect of gravity at y direction of the endpoint.

Stiffness Feasibility Region (SFR), Polytope (SFP) and Ellipsoid (SFE)

Traditionally, the stiffness ellipsoid is defined as the locus of the forces obtained $||f||$, corresponding to a deformation of unit norm. The directions of the principal axes of the stiffness ellipsoid are given by the set of orthonormal output vectors of the singular value decomposition (SVD) of this ratio, while their magnitudes are given by reciprocal of the corresponding singular values (the stiffness ellipsoid for the two-link example is illustrated in Fig. 2, most right plot).

It is important to note that the stiffness ellipsoid only conveys a "local" picture of the operational stiffness, i.e. for bounded forces and displacements that do not result in the saturation of joint actuation drives. If larger displacements are applied, however, at a certain point the manipulator will get out of the feasibility boundaries in joint torques. Indeed, for a displacement profile with a growing norm, we will realize families of growing force ellipsoids which at some point will get cut by a boundary region at different places. For instance, if we plot the locus of $||f||$ for the two-link example for different scales of the unit circle displacement profile, we realize that the ellipsoids are cut by two non-polytopic profiles corresponding to the task space force boundaries of the manipulator in configurations A and B (Fig. 4, left and right plot, respectively). In addition, the translational effect of gravity, which varies due to the change in robot configuration, will also contribute to the modifications in the geometry of such a boundary region. This is generally an undesired effect since it will influence symmetric properties of the SFR with respect to the initial equilibrium point.

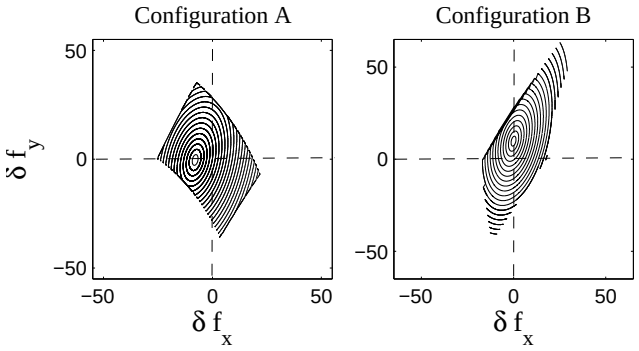

Fig. 4: The locus of $||f||$ for the growing displacement norm for the two-link manipulator in configuration A (left plot), and B (right plot) hit the limits caused by two configuration dependent force boundaries. The spatial translation of the centre of the ellipsoids w.r.t. the origin can be observed in the plots.

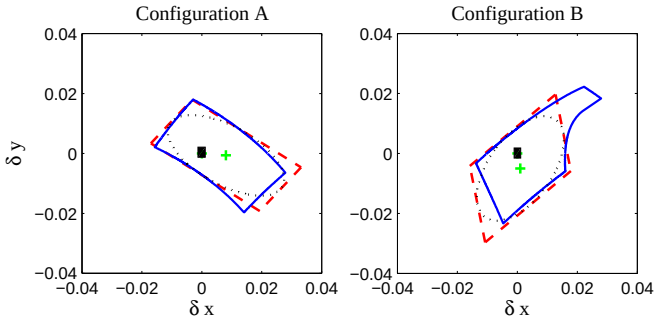

Fig. 5: Blue (solid) plots illustrate the stiffness feasibility regions (SFRs) for configuration A (left) and B (right), while corresponding polytopes are plotted in red (dashed). Stiffness feasibility ellipsoids (SFEs) are plotted in black (dotted), for both configurations. The units are in [m].

Stiffness feasibility region (SFR) is here defined by a (non-polytopic) boundary in the space of Cartesian displacement that corresponds to the maximum allowable deviation from the initial equilibrium point. Overreaching this boundary signifies that at least one of the actuators has exceeded the limits in the space of joint torques and as a consequence, the generated restoring force profile is different from the desired one. The SFRs for the two-link example in configuration A (left plots) and B (right plots) are illustrated in Fig. 5 in blue (solid).

Although SFR provides the most accurate representation of the imposed performance limits of a Cartesian stiffness controller, its calculation is computationally expensive[4], thus not suitable for real-time applications. Alternatively, the stiffness feasibility polytope (SFP) can be computed by projecting the force polytope [10] of the manipulator in a certain configuration into the space of Cartesian displacements. To that end, we first define a proper scaling of the joint torques[5]

$$\hat{\tau} = W_\tau \tau, \tag{5}$$

where $W_\tau = \text{diag}[\frac{1}{\tau_{lim_1}} \; \frac{1}{\tau_{lim_2}} \; \dots \; \frac{1}{\tau_{lim_n}}]$, and τ_{lim_i} denote the torque limit of the joint number i, that is $|\tau_i| \leq \tau_{lim_i}$. The SFP is defined as

$$\delta x \mid |\hat{\tau}|_\infty \leq 1, \tag{6}$$

with $|\,|_\infty$, denoting the infinity norm. As a result, in order to check if δx is within the SFP, n inequalities must be examined. In addition, one possible computational difficulty in the computation of the SFP lies in transforming the halfspace representation (H-representation) of the polytope to vertex representation (V-representation) [10], [13].

To simplify this problem, the L_∞ norm can be replaced by the L_2 norm to reduce the number of inequalities to one. Using the definition of the force manipulability ellipsoid [8], i.e. $|\hat{\tau}|_2 \leq 1$ we have

$$[W_\tau(J^T(q)f + \tau_g)]^T [W_\tau(J^T(q)f + \tau_g)] \leq 1, \tag{7}$$

with τ_g being the gravitational vector where $\tau_g = J^T(q)G_q$, we can write

$$(f + G_q)^T J(q) W_\tau W_\tau J^T(q)(f + G_q) \leq 1, \tag{8}$$

which under the mapping $f = K_c \delta x$ becomes

$$(\delta x + K_c^{-1} G_q)^T K_c J(q) W_\tau W_\tau J^T(q) K_c (\delta x + K_c^{-1} G_q) \leq 1. \tag{9}$$

The set of orthonormal outputs of the SVD of $K_c J(q) W_\tau$ indicate the direction of the principal axes of the stiffness feasibility ellipsoid (SFE), with the magnitudes calculated by the reciprocal of the corresponding eigenvalues. The term $K_c^{-1} G_q$ indicates a pure translation in the space of Cartesian displacements. The SFP (red, dashed) and SFE (black, dotted) for the two-link manipulator in configuration A (left) and B (right) are illustrated in Fig. 5. The approximation is more accurate near the axes of the ellipsoids, and less accurate away from them (the intuition is to approximate a unit ball under L_∞ norm, with a unit ball under L_2 norm). The spatial translation of the regions due to the effect of gravity can be observed by comparing the centres of initial (rectangle) and translated (cross) ellipsoids. Results explain that even though both configurations achieve a similar end-point stiffness matrix, their capabilities to confront external force/displacement differ.

III. Interaction Boundaries of the Cartesian Force and Stiffness Control – Redundant Case

The transformation between the joint and task spaces in a redundant manipulator does not ensure the uniqueness of the joint torque solution for a given task space force [6]. In this case, the minimization of the norm $\|\tau - \tau_g - J^T(q)f\|$, is commonly carried out by using the pseudo-inverse solution,

[4]For example, the calculation of the SFR using (4) for the two-link manipulator in configuration A took 1.12 seconds (to sweep the whole space), compared to the SFE (described next) that required 0.0013 seconds to be computed, in MATLAB.

[5]Non-symmetric boundaries of the joint torques can be treated with a proper mapping to result in a symmetric inequality [12].

[6]In redundant manipulators, the joint torques that can be used to produce a given Cartesian force vector are not unique. The joint torque vector $\tau = J^T(q)f$ represents one of these solutions. $f = J^{+T}(q)(\tau_g)$ with $J^+(q)$ a dynamically consistent generalized inverse of the Jacobian matrix corresponds to the solution that minimizes the robot's kinetic energy [14].

that is $f = J^{+T}(q)(\tau - \tau_g)$. However, the only condition ensuring that this norm equals zero, is that the torque vector $\tau - \tau_g$ is associated to the image of the Jacobian transpose [10], [15]. For this reason, to account for the task space performance limits of the redundant manipulator for a given torque boundary, only vector of joint torques that do not generate internal motions must be taken into account. This will produce reduced torque boundary region, which is basically the intersection of the joint torque boundary region (including the effect of gravity) with the image of $J^T(q)$.

Another issue in computation of the force boundary region for a redundant manipulator is that any applied displacement in the task space can be transformed into non-unique solutions in the space of joint velocities. This indicates that the chosen policy regarding the update of the joint velocities can potentially revise the resulting interaction boundaries of the Cartesian stiffness control to realize a minimally translated and task-appropriate geometry of the SFR. In this direction, due to the complexity of the SFR and SFP calculations for real-time applications, we compute the SFE by transforming the unit sphere in joint torque space into the task space and calculate its intersection with the image of the Jacobian transpose. It is well known (see e.g. [10]) that such a transformation can be performed by J^+J which leads to a similar equation as in (9), for a redundant manipulator[7], since $JJ^+JJ^T = JJ^T$.

IV. Enhancing the SFR of the Cartesian Stiffness Controller through Optimal Redundancy Resolution

As mentioned earlier, stiffness feasibility ellipsoid is a fast and intuitive tool that conveys some information on the space of maximum allowable deviation from the initial equilibrium point of a compliant robot. Especially, the directions of the maximum/minimum allowable displacement and the isotropy index (ratio between the maximum and the minimum axis [16]) of the ellipsoid are profitable properties which can provide insight into the role of robot configuration in Cartesian stiffness control capabilities. For instance, if the maximum axis of the realized SFE is elongated towards the direction of the external disturbance, the robot's Cartesian stiffness controller will be able to encounter larger deformation/force profiles prior to the occurrence of actuation torque saturation.

Our objective in this section is to explore the role of on-line redundancy resolution techniques in enhanced interaction performance of the Cartesian stiffness controllers: first, we propose an algorithm to adjust robot redundancy to maximally align the direction of the maximum axis of the SFE with the external disturbance. Next, we explore the role of robot configuration to weaken the effect of gravity on the SFE's spatial translation. A modest acquaintance with the subjects in Cartesian impedance control of torque controlled robots (e.g. see [2]) and the underlying redundancy resolution [17] is required for a better comprehension of the following section.

[7]The torque non-symmetric scaling can be performed by introducing the scaled Jacobian as $\tilde{J}^T(q) = W_\tau J^T(q)$ [10].

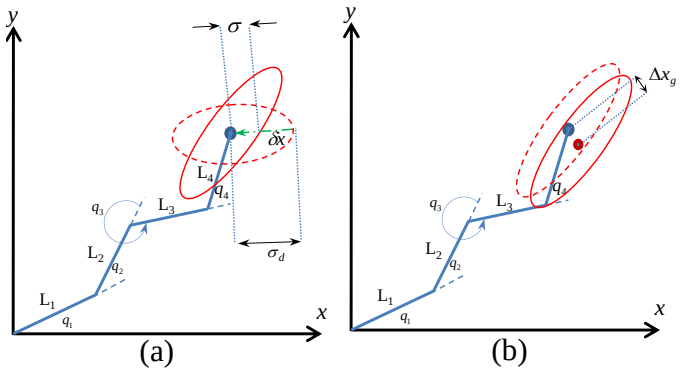

Fig. 6: 4-link planar manipulator. The SFEs are plotted in solid (realized) and dashed (desired) which correspond to a similar Cartesian stiffness matrix, but different interaction performances regarding the task space boundaries: the desired SFE is defined by (a) elongating the direction of the maximum axis of the SFE with the direction of the external disturbance, and (b) minimizing the effect of gravity in spatial translation and geometric variations of the SFE. In general, the overall geometry of the initial and optimized SEFs are different.

A. Optimizing the SFR geometry

Consider a redundant robot subject to a certain boundary in the space of joint torques. To realize a Cartesian stiffness matrix K_{c_d}, the desired joint torque vector τ_d is calculated by

$$\tau_d = \tau_{c_d} + \tau_{N_d}, \tag{10}$$

with τ_{c_d} and τ_{N_d}, corresponding to the Cartesian stiffness and null space torque vectors, respectively.

Now assume that a disturbance profile in a particular direction δx, is being applied to the e-e of the robot in a certain configuration (e.g. the four-link planar robot as illustrated in Fig. 6. a, with the SFE depicted in solid red). The length of the vector from the origin to the surface of the ellipsoid in the direction of $\frac{\delta x}{\|\delta x\|}$ specifies the maximum allowable e-e displacement prior to the actuation saturation. To compute this vector ($\sigma \in \mathbb{R}^6$), following a similar technique as described in [18], we can write

$$\left(\sigma \frac{\delta x}{\|\delta x\|}\right)^T K_c\, J(q)\, W_\tau^2\, J^T(q)\, K_c \left(\sigma \frac{\delta x}{\|\delta x\|}\right) = 1, \tag{11}$$

with $\|.\|$ denoting the vector norm operator. Solving for σ we obtain

$$\sigma = \left(\frac{\delta x^T}{\|\delta x\|} K_c\, J(q)\, W_\tau^2\, J^T(q)\, K_c \frac{\delta x}{\|\delta x\|}\right)^{\frac{-1}{2}}. \tag{12}$$

To enlarge the maximum allowable displacement profile (σ), we define the cost function

$$V_{ge} = \sum_{i=1}^{l} {\sigma_i}^2 \tag{13}$$

and *maximize* it by projecting its gradient into a dynamically consistent null space of the Jacobian transpose,

$$\delta\tau_{N_d} = [I - J^T(q)\tilde{J}^T(q)]\frac{\partial V_{ge}(q)}{\partial q}, \tag{14}$$

where I and l denote the identity matrix and the considered number of axes in the SFE (here l = 6), respectively. σ_i corresponds to the i^{th} component of vector σ. The above notations are calculated using the manipulator mass matrix $M(q)$, and Jacobian as follows

$$\begin{aligned} \tilde{J}(q) &= M^{-1}(q)\, J^T(q)\, \hat{M}(q), \\ \hat{M}(q) &= [J(q)\, M^{-1}(q)\, J^T(q)]^{-1}. \end{aligned} \tag{15}$$

The resulting null space torque profile (τ_{N_d}) will modify the geometry of the SFE, eventually coinciding its major axis with the direction of the applied displacement (Fig. 6. a, ellipsoid with dashed line where the maximum allowable displacement profile is illustrated by σ_d). Consequently, the command for the motor torque τ_m can be calculated as

$$\tau_m = \tau_d - K_\tau(\tau - \tau_d) - K_{\dot{\tau}}\dot{\tau}, \tag{16}$$

with positive definite controller matrices K_τ and $K_{\dot{\tau}}$, and $\dot{\tau}$ denoting the torque derivative. It has been demonstrated that the implementation of (16) can stabilize the torque dynamics around the equilibrium point $\tau = \tau_{d_k}$ [19], with τ_{d_k} being updated using (4) and (14).

It is important to note here that, since the SFE and its major axes directions are updated at each iteration of (14), we expect to achieve a desirable elongation of the maximum displacement region on the SFR towards the direction of the external disturbance.

B. Minimizing the gravity effect on the SFR translation and geometry

A similar technique can be used to reduce the effect of gravity on the translation (Δx in Fig. 6. b) of the achieved SFR in the task space. To do so, we calculate $\delta\tau_{N_d}$ by defining the cost function

$$V_t = \Delta x_g^T \Delta x_g, \tag{17}$$

with $\Delta x_g = K_c^{-1} G_q$, and implement a similar update law as in (14). Iterative *minimization* of V_t will contribute to the reduction of the spatial translation of the SFE and the SFR, as a consequence.

In case of the robots with high degrees of freedom (dof), such as humanoids, both the above costs can be minimized using a priority based optimization algorithm or by defining an overall cost function V_O, using a weighted (o_1 and o_2) average of V_{ge} and V_t

$$V_O = o_1 V_{ge} + o_2 V_t. \tag{18}$$

V. Results

A. Simulation Results: Four Link Manipulator

In this section, we evaluate the efficiency of the proposed algorithms for the 4-link planar redundant robot in Fig. 6. The aim is to achieve a desired Cartesian stiffness matrix, subject to specific boundaries in the space of joint torques: $|\tau_1| \leq 5\ Nm$, $|\tau_2| \leq 4\ Nm$, $|\tau_3| \leq 3\ Nm$, and $|\tau_4| \leq 2\ Nm$. $K_{c_{des}}$ is considered similar to the 2-link example. Links are assumed to have the same length, that is $0.2m$. The mass (m) of each link is assumed to be a point mass and located at the centre of each link, with $m = 2.5$ Kg. The position of the e-e is assumed to be fixed on the plane.

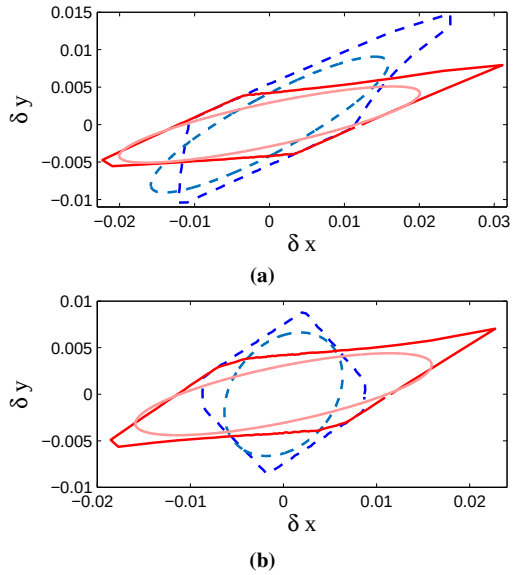

Fig. 8: SFR (dark) and SFE (light) for initial (blue, dashed) and final (red, solid) configurations A(a) and D(b) in Fig. 7. In both plots the external disturbance is applied along x direction. The units are in [m]. The ratios between the magnitude of the maximum axis of the SFE and SFR are a) 0.64 (initial) and 0.65 (final), and b) 0.78 (initial) 0.68 (final).

The first set of simulation experiments evaluates the use of the proposed redundancy resolution technique in enhanced capabilities of the manipulator to confront higher disturbance force/displacement profiles. This is achieved by maximal alignment of the major axis of the realized SFE with the direction of the external disturbance. As seen in the plots, starting from any initial configuration (Fig. 7 A-C, dashed plots), for a given external disturbance vector, (δx, Fig. 7 A-C, green arrows), and $K_{c_{des}}$, the manipulator configuration is adjusted (Fig. 7 A-C, solid plots) to align as much as possible the initial SFE's major axis (Fig. 7 A-C, blue-dotted) with the direction of external disturbance. Resulting SFEs are illustrated in solid red.

Second set of simulations aims at minimizing the translational shift of the SFE due to the effect of gravity, in addition to the alignment of the SFE's major axis with the direction of the disturbance. Using (18) and a similar update law as (14), redundant dof of the robot are controlled to realize a new configuration (Fig. 7 D, solid lines) which contributes to the reduction of the translational effect of gravity ($\|\tau_g\|$ and $\|\Delta x_g\|$ reduced to 47% and 65% of the initial values, respectively) while extending the allowable displacement profile along the direction of the applied disturbance.

Figs. 8. a and b illustrate the calculated SFRs (dark) and SFEs (light) for configurations A and D of Fig. 7, respectively. For the sake of comparison, SFRs and SFEs for both cases are plotted in the origin. The blue (dashed) regions correspond to the initial configuration, while the red (solid) ones are realized consequent to the optimal redundancy resolution. Results suggest that

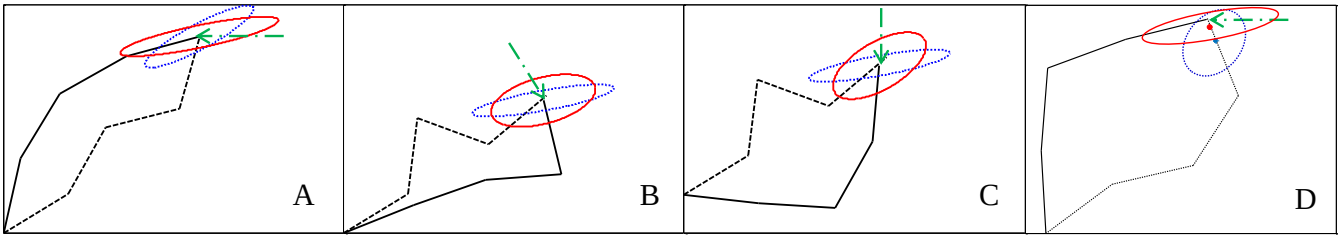

Fig. 7: Initial (dashed) and optimized (solid) configurations and the SFEs (initial: blue, optimized: red) of the four link example. The optimization algorithm utilizes the direction of the maximum SFE to orient the boundary region towards the direction of the applied disturbance (A-C). In addition, in D, the effect of gravity in translational shift of the SFE is minimized according to (18). Blue and red dots correspond to the location of the centre of initial and optimized ellipsoids, respectively.

- the proposed algorithm effectively extends the SFR towards the direction of the external disturbance; and
- even if the SFE is a rather inaccurate representation of the SFR in terms of geometry, the directions of the maximum allowable displacement in SFRs agreeably coincide with the ones in the corresponding SFE.

B. SFE vs. Force Manipulability Index

Force manipulability index (FMI) has been traditionally utilized to enhance force capabilities of a redundant manipulator to confront an external disturbance through redundancy resolution. It is commonly achieved by computing a similar cost function as in (13), while excluding K_c from the optimization process. This implies that, the effect of the desired Cartesian stiffness matrix in such an optimization is neglected (as if K_c were the identity matrix), thus for any desired K_c, results will be the same. To illustrate this point, consider the four-link manipulator in an arbitrary initial configuration (Fig. 7 A, dashed), exposed to the external disturbance vector $d = [-1\ -1]$, while realizing two Cartesian stiffness matrices

$$K_{c_a} = \begin{bmatrix} 2 & 0.4 \\ 0.4 & 0.5 \end{bmatrix} \frac{kN}{m}, \quad K_{c_b} = \begin{bmatrix} 0.5 & 0.4 \\ 0.4 & 1.5 \end{bmatrix} \frac{kN}{m}.$$

Optimization of the robot redundancy using FMI results in an identical configuration for both K_{c_a} and K_{c_b} (dashed blue 4-links in Figs. 9 a and b), whose corresponding SFRs are illustrated in the same figures (dotted-blue). Now, if a similar optimization is carried out using the SFE, the resulting configurations differ (solid black 4-links) depending on the stiffness matrix, with the SFRs illustrated in Fig. 9 in a similar order, this time in black-solid plots. These results highlight the advantage of utilizing the SFE over traditional indexes to confront large disturbance force/displacement profiles prior to the occurrence of the actuation saturation.

C. Experimental Results: Peg-in-Hole

The Peg-in-the-Hole task, a classical benchmark for spatial planning with the environmental uncertainties, was considered to evaluate the efficiency of the proposed technique in enhanced Cartesian stiffness control capabilities of a redundant, torque controlled robotic arm. In this direction, a Cartesian impedance controller (see details in [2]) was developed for the KUKA lightweight robot arm, with its torque limits being programmed one-fifth of the nominal values to simulate

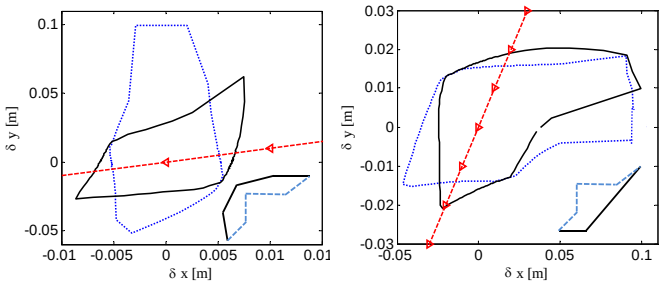

Fig. 9: SFRs of the four-link manipulator, subject to the optimization of the redundancy using FMI (blue, dotted) and SFR (black, solid) for the desired stiffness matrices a) K_{c_a} and b) K_{c_b}. The direction of the external disturbance is similar for both cases and illustrated in dashed (red) line with the arrows. The final configurations as results of optimizing FMI (blue, dotted) and SFR (black, solid) are plotted in bottom right corner of each plot.

a weaker robot. A peg (total mass: 1.6 kg) was attached to a 6 axis FT sensor (ATI Inc.), and mounted on the e-e of the robot along the z direction. A desired diagonal stiffness matrix, with $[1\ 1\ 2]\ \frac{kN}{m}$ and $[50\ 50\ 50]\ \frac{Nm}{rad}$ being the translational and rotational components, was realized using τ_{c_d} in (10). This profile achieves a stiff behavior along the peg insertion, to overcome frictional forces between the peg and the hole, while being compliant along the others, to avoid the generation of unnecessary high interaction forces.

Starting from an arbitrary configuration (e.g. see Fig. 10. A), the robot was planned to move along the direction of the hole (Fig. 10. B) to perform the assembly (insertion, 5s), to hold (2s), and to move the e-e back to its initial position (pull-off, 5s). Fig. 11 illustrates the results of this experiment. As observed in the upper plots, measured (F_z using FT sensor, plotted in solid-black) and desired ($\delta z \times K_z$, plotted in dashed-red, with $\delta z = z_m - z_d$, and $K_z = 2\frac{kN}{m}$) endpoint forces along the z direction demonstrate a linear trend until the pull-off phase, where the actuation saturation occurs (illustrated by the dashed window). As a result, the endpoint forces are different from the desired one, thus the Cartesian stiffness behaviour is not as planned. On the other hand, if the null-space torque vector is optimized to maximally align the corresponding SFE with the direction of the insertion/pull-off, the resulting configuration during assembly (Fig. 10. C)

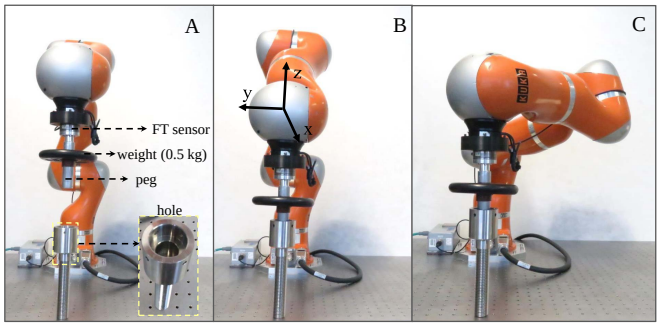

Fig. 10: KUKA robot in initial (A) and during the assembly task without (B) and with (C) the optimization of the SFE geometry.

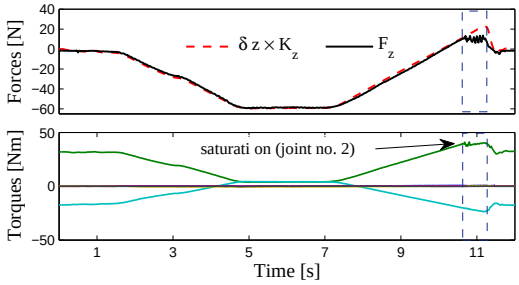

Fig. 11: Peg-in-the-Hole experimental results without the optimization of the null-space torque. Forces (measured: using FT sensor in black-solid, and desired $\delta z \times K_z$ in red-dashed) and joint torques are illustrated in upper and lower plots, respectively.

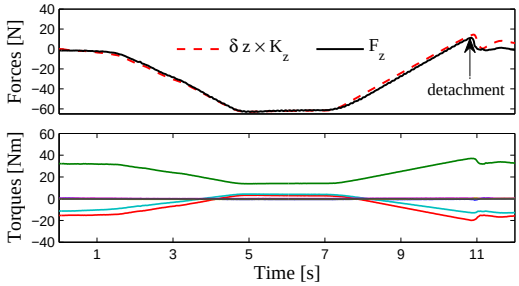

Fig. 12: Similar arrangement of the plots as in Fig. 11, this time with the optimization of the τ_{N_d} using (14).

enables the robot to confront larger external forces and as a consequence, no actuation saturation takes place and the compliant behavior of the robot is desirable (see Fig. 12). Eventually, when the peg is detached from the hole, both displacement and interaction forces converge to zero.

VI. Conclusions

This paper provided a comprehensive analysis of the task-space force/deformation behavior of redundant arms to illustrate why arm geometry plays a fundamental role in force/stiffness capabilities of a torque controlled robot. This analysis was motivated by previous studies on human motor control that demonstrated the importance of geometric factors in providing stability of hand position [5]–[7]. We introduced the notions of stiffness feasibility regions, polytopes and ellipsoids for compliant robots and explored the role of robot configuration in task-related modifications of such measures for enhanced Capabilities of the robot's Cartesian stiffness controller. In addition, the effect of gravity in geometric properties of the corresponding regions (SFE and SFR) was explored. Eventually, a control framework was proposed to regulate the null space torque and realize a task appropriate SFE (and SFR as a consequence) for an enhanced physical interaction behavior.

References

[1] F. Mussa-Ivaldi, N. Hogan, and E. Bizzi, "Neural, mechanical, and geometric factors subserving arm posture in humans," *Journal of Neuroscience*, vol. 5, no. 10, pp. 2732–2743, 1985.

[2] A. Albu-Schaffer, C. Ott, U. Frese, and G. Hirzinger, "Cartesian impedance control of redundant robots: Recent results with the dlr-light-weight-arms," in *IEEE International Conference on Robotics and Automation, 2003*.

[3] A. Pashkevich, A. Klimchik, and D. Chablat, "Enhanced stiffness modeling of manipulators with passive joints," *Mechanism and machine theory*, vol. 46, no. 5, pp. 662–679, 2011.

[4] C. Huang and I. Kao, "Geometrical interpretation of the cct stiffness mapping for serial manipulators," in *Robotics Research*. Springer, 2003, pp. 419–431.

[5] T. Milner, "Contribution of geometry and joint stiffness to mechanical stability of the human arm," *Experimental Brain Research*, vol. 143, pp. 515–519, 2002.

[6] X. Hu, W. M. Murray, and E. J. Perreault, "Biomechanical constraints on the feedforward regulation of endpoint stiffness," *Journal of neurophysiology*, vol. 108, no. 8, pp. 2083–2091, 2012.

[7] A. Ajoudani, M. Gabiccini, N. G. Tsagarakis, A. Albu-Schäffer, and A. Bicchi, "TeleImpedance: Exploring the role of common-mode and configuration-dependant stiffness," in *IEEE International Conference on Humanoid Robots*, 2012.

[8] T. Yoshikawa, "Manipulability of robotic mechanisms," *The international journal of Robotics Research*, vol. 4, no. 2, pp. 3–9, 1985.

[9] P. Chiacchio, S. Chiaverini, L. Sciavicco, and B. Siciliano, "Influence of gravity on the manipulability ellipsoid for robot arms," *Journal of dynamic systems, measurement, and control*, vol. 114, no. 4, pp. 723–727, 1992.

[10] P. Chiacchio, Y. Bouffard-Vercelli, and F. Pierrot, "Force polytope and force ellipsoid for redundant manipulators," *Journal of Robotic Systems*, vol. 14, no. 8, pp. 613–620, 1997.

[11] A. Ajoudani, N. G. Tsagarakis, and A. Bicchi, "On the role of robot configuration in cartesian stiffness control," in *Robotics and Automation (ICRA), 2015 IEEE International Conference on*. IEEE, 2015, pp. 1010–1016.

[12] A. Bicchi, C. Melchiorri, and D. Balluchi, "On the mobility and manipulability of general multiple limb robots," *Robotics and Automation, IEEE Transactions on*, vol. 11, no. 2, pp. 215–228, 1995.

[13] K. Fukuda and A. Prodon, "Double description method revisited," in *Combinatorics and computer science*. Springer, 1996, pp. 91–111.

[14] O. Khatib, "A unified approach for motion and force control of robot manipulators: The operational space formulation," *Robotics and Automation, IEEE Journal of*, vol. 3, no. 1, pp. 43–53, 1987.

[15] S. Krut, O. Company, and F. Pierrot, "Force performance indexes for parallel mechanisms with actuation redundancy, especially for parallel wire-driven manipulators," in *IEEE/RSJ International Conference on Intelligent Robots and Systems*, 2004.

[16] L. Stocco, S. Salcudean, and F. Sassani, "Fast constrained global minimax optimization of robot parameters," *Robotica*, vol. 16, no. 6, pp. 595–605, 1998.

[17] O. Khatib, "Motion/force redundancy of manipulators," in *Proceedings of Japan-USA Symposium on Flexible Automation*, vol. 1, 1990, pp. 337–342.

[18] S. L. Chiu, "Task compatibility of manipulator postures," *The International Journal of Robotics Research*, vol. 7, no. 5, pp. 13–21, 1988.

[19] C. Ott, *Cartesian impedance control of redundant and flexible-joint robots*. Springer, 2008, vol. 49.